Journal of Non-Newtonian Fluid Mechanics 308 (2022) 104882

Contents lists available at ScienceDirect

Journal of Non-Newtonian Fluid Mechanics

journal homepage: www.elsevier.com/locate/jnnfm

Effects of bulk elasticity on sheet formation and expansion

Mariana Rodríguez-Hakim[1,*], Laura Stricker[1], Jan Vermant

Department of Materials, ETH Zurich, Vladimir-Prelog-Weg 5, Zurich, 8093, Switzerland

ARTICLE INFO

Keywords:
Viscoelasticity
Impinging jets
Fluid sheets
Extensional flow
Upper convected Maxwell model

ABSTRACT

The destabilization, fragmentation, and atomization of thin fluid sheets governs processes such as the aerosolization of sneeze ejecta, agrochemical spraying, and fuel injection in liquid rocket engines. Although the evolution, stability, and breakup of fluid sheets composed of a Newtonian liquid has been extensively studied, the morphology and dynamics of viscoelastic fluid sheets remains poorly understood. This manuscript provides a theoretical and numerical framework that integrates the effects of fluid elasticity, surface tension, inertia, and viscosity to predict the morphology, velocity, and stress within stable fluid sheets composed of viscoelastic fluids as a function of the dimensionless Weber, Reynolds, and Weissenberg numbers. We find a non-monotonic behavior in the sheet's size, velocity, and stress distribution as a function of the ratio between the Weissenberg and the Weber numbers. In particular, a minimum in the sheet's size and a maximum in the stress occur when such a ratio is of the order of unity. We interpret these results as the consequence of the competing effects of the growth-favoring inertia and the restoring elastic forces acting within the sheet.

1. Introduction

The formation of thin fluid sheets and their fragmentation into sprays of droplets has many industrial and practical applications, such as fuel injection in liquid rocket engines, spin coating of substrates, and agrochemical spraying of crops [1–6]. Some applications, such as spin coating, require the existence of smooth, stable sheets that homogeneously coat the substrate; for other applications, such as crop spraying, unstable sheets that atomize into aerosols are necessary [5,6,4].

Thin fluid sheets are also present in quotidian events, such as when liquids are poured out of lipped pitchers [4] or during activities such as speaking or sneezing, where inertia flattens the expelled mucosalivary volume into a sheet-like structure [7–10]. This is accompanied by the appearance of holes and thin filaments within the sheet, which subsequently destabilize and break up into a spray of droplets [7–10].

An understanding of the dynamics of sheet formation and breakup is thus necessary to systematically control regimes of sheet stability, set desired film thicknesses for stable sheets, and tune the range of drop size distributions in atomized sprays [11,4,5,12–16]. Although the formation, morphology, and stability of Newtonian sheets is well studied, the dynamics of viscoelastic fluid sheets, such as polymeric coatings or saliva, is not yet fully understood, since the complex interplay between inertial, capillary, viscous, and elastic stresses can introduce deviations from the classical Newtonian behavior of thin fluid sheets [17–20,10].

The present work focuses on providing a physical description of stable, quasi-two dimensional sheets formed by a pair of oppositely facing impinging jets. Upon collision, the momentum transferred by the two jets results in the formation of a radially expanding sheet in the plane perpendicular to the plane of the jets [4,11,12]. The sheets are externally bounded by a thicker cylindrical rim, which can destabilize into ligaments and droplets under certain conditions [4,11,12].

The shape and size of Newtonian liquid sheets formed through the collision of laminar jets was first documented in the pioneering work of Savart in 1833 [21,22]. This system was further characterized by Magnus in 1855 [23] and subsequently in a series of works by Taylor, who measured the thickness distribution along the sheets, derived the general equations for the sheet shape, and compared the experimental results with theoretically-calculated profiles [13–16]. The thickness distribution was later determined theoretically by Hasson and Peck, assuming a plug velocity profile within the liquid jets and no dissipation of energy upon impact [12].

The sheet shape, rim position, and liquid velocity were analytically and experimentally quantified by other authors as a function of the incident jet velocity, radius, and orientation [11,4,6,24]. The size and morphology of Newtonian liquid sheets is determined by a competition between inertial forces, which drive sheet expansion and thinning, and capillary forces, which limit the sheet's surface area and radial expansion. Thus, the stationary length and width of stable Newtonian sheets scale with the Weber number [11,16,5,25].

Newtonian sheets become unstable when inertial forces exceed a critical value [11]. The ratio and magnitude of capillary, inertial, and

* Corresponding author.
E-mail address: mariana.rodriguezhakim@mat.ethz.ch (M. Rodríguez-Hakim).
[1] Both authors contributed equally to this work.

https://doi.org/10.1016/j.jnnfm.2022.104882
Received 11 May 2022; Received in revised form 12 July 2022; Accepted 13 July 2022
Available online 18 July 2022

viscous forces, quantified by the dimensionless Weber and Reynolds numbers, determine the morphological and dynamic characteristics of the sheet and rim destabilization [5,4]. A linear stability analysis was carried out by Bremond and Villermaux, who revealed that capillary Rayleigh–Plateau instabilities drive fluctuations in the rim that eventually grow and destabilize into ligaments [11]. Other breakup regimes have been mapped by several authors [5,4,3,26,27], revealing a rich set of instabilities such as a periodic "fishbone"-type rim fragmentation, the appearance of expanding holes within the films, and the formation of aerodynamic or hydrodynamic waves that result in the full atomization of the liquid sheets. High fidelity numerical simulations of Newtonian jets over a range of stability conditions, ranging from stable films to atomizing sheets, have also been carried out and the resulting morphologies compared to the experimentally observed structures [6].

Although the morphology and dynamics of stable and unstable Newtonian liquid sheets formed by a pair of impinging jets has been extensively studied through a combination of experimental, theoretical, and numerical approaches, only a handful of works have investigated viscoelastic sheet formation [18,20,28,19,29,17,30]. In particular, numerical works on sheets formed by the discharge of liquid from thin slits [17,18] and experiments on worm-like micelles [19] and dissolved polymers [28,29] revealed that a higher elastic modulus results in the formation of smaller sheets [17,18]. Hence, it is expected that elasticity acts alongside capillarity to resist the radial spread of the film and deter sheet breakup by inducing stabilizing tensile stresses. However a quantitative study of the thickness, velocity, and stress distributions within liquid sheets formed by colliding impinging jets as a function of the fluid's elasticity is still lacking.

The present work aims at advancing our understanding of stable liquid sheets composed of viscoelastic liquids formed by the collision of two impinging jets. We revisit the general set of governing equations previously derived by Entov et al. for sheets formed by the discharge of liquids from thin slits [17], by adapting them to the case of impinging jets. Hence, we develop a set of governing equations and boundary conditions to predict the thickness, velocity, and stress distributions within liquid sheets as a function of the fluid's elasticity, viscosity, inertia, and surface tension, as quantified via the dimensionless Weber (We), Reynolds (Re), and Weissenberg (Wi) numbers. We conduct a systematic parametric study of the three dimensionless numbers and elucidate their role in determining the shape, size, velocity, and stress distribution within the films. To the best of our knowledge such a study has not yet been conducted.

The Newtonian asymptotic limit of the sheet's size is controlled by the Weber number, which quantifies the ratio of inertial to capillary stresses, in line with previous works [26]. For viscoelastic sheets, the Weissenberg number determines to what extent elastic forces contribute to the buildup of extensional stresses throughout the film. We find that the ratio between the Weissenberg and the Weber numbers (Wi/We), hereafter referred to as the modified Weissenberg number (Wi^*), reflects the ratio of the solution's elastic relaxation time divided by the convective process timescale. A non-monotonicity in sheet size and stress is revealed for Wi^* on the order of unity, elucidating that the largest deviations from Newtonian behavior occur when the relaxation time of the solution equals the time required for a fluid element to traverse the extent of the film. The magnitude of this non-monotonicity is controlled by the Reynolds number, which expresses the relative importance of inertial to viscous effects.

Overall, our work discloses the intricate interplay of physical forces that leads to previously unexplored morphologies and stress distributions within viscoelastic liquid films, expanding our understanding of how the presence of viscoelastic materials influences sheet formation, expansion, and thinning.

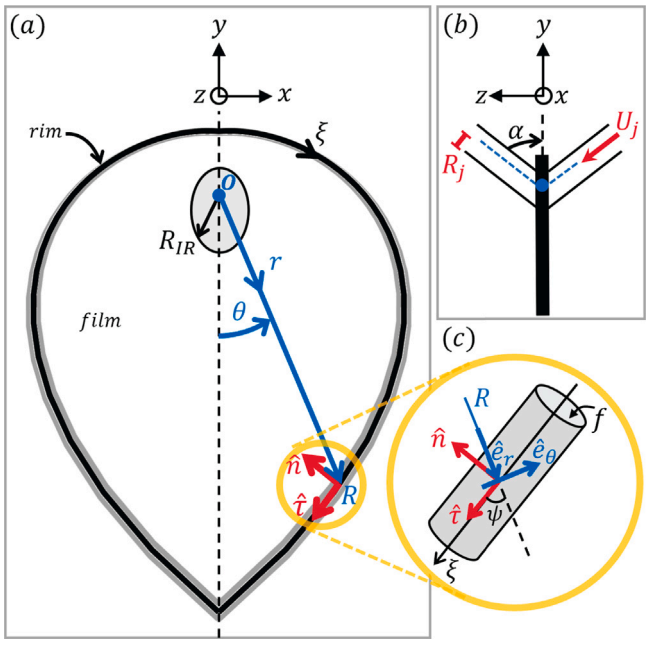

Fig. 1. Schematic of the sheet geometry. (a) Front view. Upon impingement of two identical liquid jets, a flat fluid sheet is formed along the x–y plane. The sheet is divided into two sections: a quasi-two dimensional film (white) and a cylindrical rim (gray) that bounds the edge of the film. The gray ellipse marks the jet impingement region at $r = R_{IR}$ and the inner boundary of the film, which is described using a cylindrical coordinate system $(r - \theta)$. The rim position is characterized using a parameterized coordinate system $(\xi - \psi)$, where the normal $\hat{\boldsymbol{n}}$ and tangent $\hat{\boldsymbol{\tau}}$ vectors are depicted in red. (b) Side view. Liquid sheets are formed by two identical liquid jets of radius R_j and average velocity U_j oriented at an angle α with the y-axis. (c) Magnification of a section of the rim. The cylindrical rim runs along the ξ axis and has a cross-sectional area f. The relationship between the relevant unit normal vectors is shown, where ψ is the angle formed between $\hat{\boldsymbol{\tau}}$ and $\hat{\boldsymbol{e}}_r$.

2. Physical modeling of viscoelastic fluid sheets

We consider a system where a liquid sheet is formed through the collision of two identical liquid jets of radius R_j and average velocity U_j oriented along the $y - z$ plane, as depicted in Fig. 1b. The jets are oriented at an angle $2\alpha = \pi/2$ with respect to each other and the system is symmetric with respect to the vertical y-axis. Hence, $\alpha = \pi/4$ is the angle formed by each jet and the vertical y-axis. Upon collision, the momentum transferred by the two jets results in the formation of a thin fluid sheet oriented along the x–y plane (Fig. 1a). The fluid sheet is divided into two sections: a thin, quasi-two dimensional film formed upon jet impingement (denoted as 'film' in Fig. 1a), and a thicker cylindrical rim that bounds the perimeter of the film (denoted as 'rim' in Fig. 1a).

This Section summarizes the dimensionless governing equations for stable sheets composed of viscoelastic liquids, namely the conservation of mass and momentum. Stresses and deformations are described by an upper-convected Maxwell constitutive model [17,18]. Simplifying assumptions on the nature of the flow and stress fields are used to cast the system of equations as two sets of ordinary differential equations (ODEs) for the film and for the rim, respectively, in order to facilitate the numerical solution. The appropriate boundary conditions for the geometry at hand are also derived here. For the interested reader, the derivations of the equations, originally proposed in the works of Entov et al. [17] and Yarin [18] for a different geometry, can also be found, revisited and adapted to the geometry at hand, in the Supplemental Material.

2.1. Film equations

A cylindrical coordinate system (r, θ, z) is used to model the film geometry, as shown in Fig. 1, with the z-axis oriented along the thickness of the sheet. Upon impingement, the jets form an ellipse in the $r-\theta$ plane, whose position is given by $r = R_{IR}(\theta)$. In this elliptical impingement region, the streamlines oriented along the jet direction are deflected towards the plane of the sheet. Of special importance is the separation streamline, which forms a stagnation point in the elliptical impingement region and divides the streamlines deflected at each angular position θ. The origin O of the coordinate system is placed at this stagnation point [11,12].

The conservation of mass and momentum determine the dimensionless thickness $2h$, velocity $\boldsymbol{U}$, and stress $\boldsymbol{\sigma}$ within the liquid film. The mass continuity and Cauchy momentum equations are written in dimensionless form as

$$0 = \boldsymbol{\nabla} \cdot \boldsymbol{U}, \tag{1}$$

$$\boldsymbol{U} \cdot \boldsymbol{\nabla} \boldsymbol{U} = \boldsymbol{\nabla} \cdot \boldsymbol{\sigma}. \tag{2}$$

All equations in this manuscript are rendered dimensionless by scaling the lengths and distances with the jet radius R_j, the velocities by the average jet velocity U_j, and the stresses by the inertial stress scale ρU_j^2.

The total stress $\boldsymbol{\sigma}$ in the film is written as the sum of an isotropic pressure $(P\boldsymbol{\delta})$, with $\boldsymbol{\delta}$ the identity matrix, and a deviatoric stress, which is expressed as the sum of a polymeric $(\boldsymbol{T}^P)$ and a Newtonian solvent $(2\boldsymbol{D}/Re_s)$ contribution, as follows:

$$\boldsymbol{\sigma} = -P\boldsymbol{\delta} + \boldsymbol{T}^P + \frac{2}{Re_s}\boldsymbol{D} \approx -P\boldsymbol{\delta} + \boldsymbol{T}^P, \tag{3}$$

$$\text{where} \quad \boldsymbol{D} = \frac{1}{2}\left(\nabla \boldsymbol{U} + \nabla \boldsymbol{U}^T\right). \tag{4}$$

$Re_s = \rho R_j U_j / \eta_s$ is the Reynolds number of the Newtonian solvent, η_s is the solvent viscosity, ρ is the fluid density, and $\boldsymbol{D}$ is the rate-of-strain tensor. The quasi-two dimensional sheets in this manuscript are formed by the inertia supplied by the pair of impinging jets, such that $Re_s \gg 1$. Additionally, the solvent contribution to the extra stress is neglected, effectively attributing any deviatoric stress buildup in the viscoelastic sheets to the presence of the polymer. This assumption is justified by the fact that sheets formed by impinging jets composed of Newtonian fluids are always considered stress-free.

The upper-convected Maxwell (UCM) model relates the polymeric stress contribution to the velocity gradients in the fluid,

$$\boldsymbol{T}^P + Wi\, \boldsymbol{T}^{P(1)} = \frac{2}{Re}\boldsymbol{D}, \tag{5}$$

$$\text{where} \quad \boldsymbol{T}^{P(1)} = \frac{D\boldsymbol{T}^P}{Dt} - (\boldsymbol{\nabla U})^T \cdot \boldsymbol{T}^P - \boldsymbol{T}^P \cdot (\boldsymbol{\nabla U}), \tag{6}$$

where $\boldsymbol{T}^{P(1)}$ is the upper-convected derivative of the polymeric stress.

In Eqs. (5)–(6), we have introduced the following dimensionless parameters:

$$Re = \frac{\rho U_j R_j}{\eta_P} \qquad \text{(Reynolds number)}, \tag{7}$$

$$Wi = \frac{\lambda U_j}{R_j} \qquad \text{(Weissenberg number)}, \tag{8}$$

where η_P corresponds to the polymer contribution to the zero-shear viscosity. The Reynolds number has its usual meaning of characterizing the ratio between inertial and viscous stresses. While inertia is the dominant force driving the flow and, hence, the sheet's growth, viscosity acts as a dissipative growth-mitigating mechanism. The Weissenberg number is the ratio between the polymer's longest relaxation/retardation time λ and a characteristic time of the process, related to inertia, R_j/U_j. The exact interpretation of Wi will become clearer in the discussion below, as we will show how it determines whether elastic effects play a dominant role in shaping the stress distribution and morphology of the sheets.

The present analysis is developed using the UCM model as the constitutive model, in view of its simplicity, its reduced number of parameters, and its ability to capture the overall behavior of viscoelastic fluids [31]. The mathematical framework presented in this manuscript can easily be adapted to other more elaborate nonlinear constitutive models that may be more suitable to capture conditions where shear thinning behavior or high strain rates occur.

Eqs. (1), (2) and (5) are coupled partial differential equations and can be solved to yield the velocity and stress distribution throughout the film. Following the work of Entov et al. [17] and Yarin [18], a series of simplifying assumptions are made in order to cast the system of equations as a set of nonlinear ODEs. This remainder of this Section lists the main assumptions and the final form of the simplified film equations. A full derivation is made accessible in the Supplemental Material.

Due to the thinness of the sheet, the governing equations are simplified following the auspices of the lubrication theory [32,33]. Furthermore, as with Newtonian flows, it is assumed that the flow inside the film is vorticity-free. These assumptions imply that, to leading order, the film adopts a unidirectional velocity profile given by

$$\boldsymbol{U} \approx U_r(r, \theta)\ \hat{\boldsymbol{e}}_r, \tag{9}$$

where the radial flow has a thickness-averaged, plug-type profile. Using this definition for $\boldsymbol{U}$, the film continuity equation (Eq. (1)) simplifies to the algebraic expression

$$C_1(\theta) = rU_r h, \tag{10}$$

where $C_1(\theta)$ is a function of θ only, and U_r and h are evaluated at r. An expression for $C_1(\theta)$ in terms of the θ and the impingement angle α is derived later in the text (see Eq. (24)).

Due to the extensional nature of the flow field within the expanding liquid film, extensional stresses dominate over shear stresses. Moreover, a stress-free boundary condition is applied at the liquid–air interface, $\boldsymbol{\sigma}(r, \theta, z = \pm h) = 0$, where $\boldsymbol{\sigma}$ is the total stress tensor. Hence,

$$\boldsymbol{\sigma} \approx \sigma_{rr}(r, \theta)\ \hat{\boldsymbol{e}}_r\hat{\boldsymbol{e}}_r + \sigma_{\theta\theta}(r, \theta)\ \hat{\boldsymbol{e}}_\theta\hat{\boldsymbol{e}}_\theta + \sigma_{zz}(r, \theta)\ \hat{\boldsymbol{e}}_z\hat{\boldsymbol{e}}_z, \tag{11}$$

where σ_{rr}, $\sigma_{\theta\theta}$, and σ_{zz} are the thickness-averaged, extensional components of the stress tensor.

Following the aforementioned assumptions, the r-component of the Cauchy momentum equation (Eq. (2)) reduces to

$$U_r rh\frac{\partial U_r}{\partial r} = \frac{\partial\left(rh\sigma_{rr}\right)}{\partial r} - \sigma_{\theta\theta}h. \tag{12}$$

Due to the stress-free boundary condition, to leading order the z-component reduces to the expression

$$\sigma_{zz} = 0. \tag{13}$$

Using this result and Eq. (3), an expression for the isotropic pressure can be obtained, where

$$P = T^P_{zz}. \tag{14}$$

Thus, the relevant components of the total stress tensor can be entirely written in terms of the deviatoric stresses, as

$$\sigma_{rr} = T^P_{rr} - T^P_{zz}, \tag{15}$$

$$\sigma_{\theta\theta} = T^P_{\theta\theta} - T^P_{zz}, \tag{16}$$

where all stresses are thickness-averaged. Due to the number of equations and unknowns, the θ-component of the Cauchy momentum equation is not needed.

The extensional components of the UCM model evaluate to the following expressions:

$$\frac{\partial T^P_{rr}}{\partial r} = \frac{1}{U_r}\left(\frac{2}{Re\, Wi}\frac{dU_r}{dr} - \frac{1}{Wi}T^P_{rr} + 2\frac{dU_r}{dr}T^P_{rr}\right), \tag{17}$$

$$\frac{\partial T^P_{\theta\theta}}{\partial r} = \frac{1}{U_r}\left(\frac{2}{Re\, Wi}\frac{U_r}{r} - \frac{1}{Wi}T^P_{\theta\theta} + \frac{2}{r}U_r T^P_{\theta\theta}\right), \tag{18}$$

$$\frac{\partial T_{zz}^P}{\partial r} = \frac{1}{U_r}\left[-2\left(T_{zz}^P + \frac{1}{Re\,Wi}\right)\left(\frac{dU_r}{dr} + \frac{U_r}{r}\right) - \frac{1}{Wi}T_{zz}^P\right]. \tag{19}$$

The continuity equation has been used to make the substitution $\frac{\partial U_z}{\partial z} = -\frac{\partial U_r}{\partial r} - \frac{U_r}{r}$. Finally, the $r-\theta$ component of the UCM model can be used to show that U_r is independent of θ, such that $U_r = U_r(r)$.

Substituting Eq. (10) and Eqs. (17)–(19) into Eq. (12), the r-component of the momentum equation can be expressed entirely in terms of the polymer stresses and film velocity, as

$$\frac{dU_r}{dr} = \left[\frac{T_{zz}^P - T_{rr}^P}{Wi} - \frac{2U_r}{Re\,Wi\,r} + \frac{2U_r T_{zz}^P}{r} + \frac{U_r\left(T_{zz}^P - T_{\theta\theta}^P\right)}{r}\right] \left[U_r^2 - \frac{4}{Re\,Wi} - T_{rr}^P - 3T_{zz}^P\right]^{-1}, \tag{20}$$

Eqs. (17)–(20) represent a system of nonlinear first-order ODEs in terms of the radial coordinate, r. Thus, four boundary conditions are needed to solve for the film velocity U_r and the film stresses T_{rr}^P, $T_{\theta\theta}^P$, and T_{zz}^P. Following the work of Hasson and Peck [12] and Bremond and Villermaux [11], the boundary conditions are specified at the boundary of the elliptical impingement region, located at $r = R_{IR}(\theta)$.

The dimensionless function $R_{IR}(\theta)$ prescribes the location where the fluid film is formed and begins to radially expand. Following the derivation of Ref. [12], we assume that polymer stresses developing within the liquid jets prior to impingement are negligible and the jets have a plug flow profile. Thus, R_{IR} can be written as

$$R_{IR} = \frac{\sin\alpha}{1-\cos\theta\cos\alpha}. \tag{21}$$

The full derivation can be accessed in the Supplemental Material. In situations where polymer stresses within the jet (before impingement) become relevant, a shift in the position of the separation streamline may occur. A correction to account for the shift of the origin location could then be introduced in the expression for R_{IR}. We do not expect such corrections to have an impact on the physics of the problem, hence we limit the analysis to cases where such effects are negligible.

Mass and energy balances for a control volume extending from the jets up to the impingement boundary R_{IR} are set up, assuming no energy dissipation. Details concerning the definition of the control volume and the derivation of the boundary conditions can be found in the Supplemental Material. The resulting expressions provide boundary conditions for U_r and h, where:

$$U_r\Big|_{r=R_{IR}} = 1, \tag{22}$$

$$h\Big|_{r=R_{IR}} = \frac{R_{IR}}{2}\sin\alpha. \tag{23}$$

Eqs. (22) and (23) can be used to obtain the value of the unknown function $C_1(\theta)$, since the quantity rU_rh is conserved at a constant angle θ, as per Eq. (10), which subsequently evaluates to:

$$C_1(\theta) = rU_rh = rU_rh\Big|_{r=R_{IR}} = \frac{R_{IR}^2}{2}\sin\alpha. \tag{24}$$

Since the jets are freely suspended in air and have a plug flow profile, we assume that the fluid is stress-free up to the point of impingement, such that

$$T_{rr}^P\Big|_{r=R_{IR}} = T_{\theta\theta}^P\Big|_{r=R_{IR}} = T_{zz}^P\Big|_{r=R_{IR}} = 0. \tag{25}$$

The assumption of a zero-stress boundary condition is rigorously valid for freely suspended jets at a (dimensional) distance larger than $U_j\lambda$ from each other; for smaller distances, corrections accounting for residual stresses may be incorporated. However, we do not expect such corrections to significantly modify the observed trends, hence, in view of its simplicity, we constrain our study to the case of zero-stress boundary conditions.

2.2. Rim equations

The governing equations for the rim are most conveniently expressed using a parameterized (local) coordinate system, in which the $\xi-\psi$ coordinate axes are defined along the rim, as shown in Fig. 1 [11,18,17]. The following geometric relations are established between the film's cylindrical coordinate system and the rim's parameterized coordinate system, where

$$\frac{d\xi}{d\theta} = -\frac{R}{\sin\psi}, \tag{26}$$

$$\frac{dr}{d\theta} = -\frac{R}{\tan\psi}. \tag{27}$$

In this local coordinate system, the ξ-coordinate is the arc length along the rim and the ψ-coordinate is defined as the angle between the ξ- and r-coordinates. Hence, ψ quantifies the local deviation of the rim from a circle with radius R centered at the stagnation point O, which would correspond to a value of $\psi = \pi/2$. It is worthwhile to note that while the film is a 2D system in which r and θ can independently vary, the rim is a 1D system in which R (the radial position of the rim) and θ are mutually constrained through Eq. (27). In addition, the normal and tangent vectors at the rim can be defined as:

$$\hat{\boldsymbol{n}} = -\sin\psi\hat{\boldsymbol{e}}_r - \cos\psi\hat{\boldsymbol{e}}_\theta, \tag{28}$$

$$\hat{\boldsymbol{\tau}} = \cos\psi\hat{\boldsymbol{e}}_r - \sin\psi\hat{\boldsymbol{e}}_\theta, \tag{29}$$

where the ξ-coordinate is tangent to $\hat{\boldsymbol{\tau}}$.

Similarly to the film, mass and momentum balances along the rim are used to determine the rim's radial position $R(\theta)$, cross-sectional area f, velocity $\boldsymbol{U}_\xi$, and orientation ψ. The rim continuity and momentum equations are obtained by balancing the conserved quantity's influx from the sheet with its flow through a differential section of the rim.

Following Refs. [18,17,11], we assume that the rim has a circular cross-section and a plug flow profile which runs tangent to the ξ-axis, where

$$\boldsymbol{U}_\xi(\xi) = U_\xi(\xi)\,\hat{\boldsymbol{\tau}}. \tag{30}$$

Under these assumptions, the rim continuity equation becomes:

$$\frac{d\left(U_\xi f\right)}{d\theta} = -2C_1, \tag{31}$$

where C_1 is given by Eqs. (24) and (26) has been used to cast the derivative in terms of θ, since it is more convenient to express the rim equations in terms of θ rather than ξ, whose upper bound is unknown.

As in Refs. [17,18], we assume that the rim is stress-free. Thus, the rim's momentum balance is obtained by equating momentum convection due to mass influx/outflux with the momentum diffusion originating from the presence of bulk and interfacial stresses:

$$\frac{d\left(U_\xi^2 f\hat{\boldsymbol{\tau}}\right)}{d\theta} = -2C_1\boldsymbol{U} - \frac{2C_1}{U_r\sin\psi}\hat{\boldsymbol{n}}\cdot\boldsymbol{\sigma} - \frac{2}{We}\frac{R}{\sin\psi}\hat{\boldsymbol{n}}. \tag{32}$$

The dimensionless Weber number has been introduced in the stress balance for the rim, where

$$We = \frac{\rho U_j^2 R_j}{\gamma} \qquad \text{(Weber number)}, \tag{33}$$

and γ is the interfacial tension between the liquid and the air. The Weber number quantifies the ratio of inertial forces, which drive sheet formation and expansion, and capillary forces, which limit the areal extent of the film.

The tangential and normal components of the momentum balance can be obtained by dotting Eq. (32) with $\hat{\boldsymbol{n}}$ and $\hat{\boldsymbol{\tau}}$, respectively:

$$\frac{d\left(U_\xi^2 f\right)}{d\theta} = \left[-\frac{2C_1}{U_r}\cos\psi\left(U_r^2 + T_{\theta\theta}^P - T_{rr}^P\right)\right]_{r=R(\theta)}, \tag{34}$$

$$\frac{d\psi}{d\theta} = \frac{2}{U_\xi^2 f}\left[-\frac{C_1}{U_r \sin\psi}\left(T_{rr}^P \sin^2\psi + T_{\theta\theta}^P \cos^2\psi - T_{zz}^P\right) + C_1 U_r \sin\psi - \frac{R}{We\ \sin\psi}\right]_{r=R(\theta)} + 1, \tag{35}$$

where the film velocity and stresses are evaluated at the rim's radial position $R(\theta)$, and are given by the solutions of the film equations. Eqs. (27), (31), (34), and (35) thus represent a system of ODEs for the rim in terms of the angular coordinate θ.

The boundary conditions for the rim variables at the stagnation point $\theta = \pi$, i.e the most upstream position of the rim, are:

$$\psi\Big|_{\theta=\pi} = \pi/2, \tag{36}$$

$$U_\xi\Big|_{\theta=\pi} = 0, \tag{37}$$

$$R\Big|_{\theta=\pi} = R_0 = We\, C_1^*\left[U_r - \frac{T_{rr}^P - T_{zz}^P}{U_r}\right]_{r=R_0}, \tag{38}$$

$$\text{where } C_1^* = C_1\Big|_{\theta=\pi} = \frac{\sin^3\alpha}{2(1+\cos\alpha)^2}, \tag{39}$$

where R_0 is the radial position at the stagnation point. The right-hand-side (RHS) of Eq. (38) is derived by evaluating (Eq. (35)) at $\theta = \pi$, by accounting for $d\psi/d\theta|_{\theta=\pi} = 0$.

3. Numerical model

We outline here the method used to derive the numerical solution of the system of ODEs. Note that the equations for the film can be solved independently of the equations for the rim, but not vice-versa. The system of ODEs describing the rim variables is indeed coupled to the film equations, via the values of the film variables (namely the radial velocity and the stresses) at the rim location. Since the rim equations (Eqs. (27), (31), (34), and (35)) become singular at $\theta = \pi$, we modify the boundary conditions. In particular, following the strategy outlined in [18,11], we move the boundary condition slightly downstream, at a rim position $\theta = \pi - \epsilon$, where ϵ is small enough that one can still consider

$$\psi\Big|_{\theta=\pi-\epsilon} = \psi\Big|_{\theta=\pi} = \pi/2, \tag{40}$$

$$r\Big|_{\theta=\pi-\epsilon} = r\Big|_{\theta=\pi} = R_0. \tag{41}$$

The remaining boundary conditions at the new location are derived by means of a local energy and mass balance, whose details can be found in the Supplemental Material,

$$(U_\xi f)_{\theta=\pi-\epsilon} = 2\epsilon C_1^*, \tag{42}$$

$$(U_\xi^2 f)_{\theta=\pi-\epsilon} = 2\epsilon C_1^* U_r\Big|_{R_0}. \tag{43}$$

In order to solve the system of ODEs describing the system, we first integrate the film equations (Eqs. (17)–(20)) along the radial direction, starting from $r = R_{IR}$, for $\theta = \pi$. Thus, we derive the position of the stagnation point R_0 by means of an iterative procedure. The procedure is repeated until the residual between the left-hand-side (LHS) and the right-hand-side (RHS) of Eq. (38) is $|\text{LSH} - \text{RHS}| \leq \text{tol}$, with $\text{tol} = 10^{-8}$ the required tolerance. We then use the derived value of R_0 to evaluate the initial boundary conditions for the rim's equations and we proceed by numerically integrating Eqs. (27), (31), (34), and (35) in the range $\theta \in [\pi - \epsilon, 0]$. As the main integration of the rim equations is performed along θ, the required values of $U_r, T_{rr}^P, T_{\theta\theta}^P$, and T_{zz}^P at the rim position $r = R$ (see Eqs. (34) and (35)) are calculated by separately integrating the film equations (Eqs. (17)–(20)) starting from $r = R_{IR}$ up to $r = R$. All integrations are performed with an explicit six-stage fifth-order Runge–Kutta method [34], implemented by means of the *ode45* Matlab subroutine [35].

4. Results

We now establish how viscous, inertial, capillary, and elastic effects influence the size, velocity, and stress distribution within the liquid film and rim, and to what extent sheets formed by viscoelastic liquids differ from their Newtonian counterparts. For this purpose, we conduct a parametric sweep in terms of the relevant dimensionless parameters that appear in the governing equations for the sheet and rim.

The size of Newtonian sheets is solely determined by We. Hence, it is expected that this parameter governs the asymptotic behavior in the limit of Newtonian sheets. However, for viscoelastic sheets, three dimensionless parameters - Re, Wi, and We - capture the interplay between inertial, capillary, viscous, and elastic forces that govern the sheet morphology and dynamics. The Weber number (We, Eq. (33)) represents the competition between inertial driving forces and capillary restoring forces, while the Reynolds number (Re, Eq. (7)) reflects the ratio of inertial and viscous driving forces. The Weissenberg number (Wi, Eq. (8)) itself is of more difficult interpretation, since it does not represent a ratio of physically relevant quantities within the liquid sheet.

However, the dimensionless film and rim equations can be rescaled in order to determine the most relevant combinations of dimensionless groups governing their solution (the rescaled ODEs and boundary conditions are provided in the Supplemental Material). From the rescaled equations, we expect the most relevant parameter in determining the qualitative behavior of the sheet dynamics and morphology to be the modified Weissenberg number, $Wi^* = Wi/We$. Unlike for Wi, the physical interpretation of Wi^* is readily established. Such a parameter can indeed be written as

$$Wi^* = \frac{Wi}{We} = \frac{t_{rel}}{t_{conv}} = \frac{\lambda\gamma}{\rho U_j R_j^2} \quad \text{(modified Weissenberg number)}. \tag{44}$$

Hence, Wi^* can be interpreted as the ratio of the solution's relaxation time $t_{rel} = \lambda$ divided by the convective (or process) timescale $t_{conv} = \rho U_j R_j^2/\gamma$. The relaxation time of the solution t_{rel} quantifies the time required for a polymer element to relax back to an equilibrium, un-stretched state following a given deformation, and measures the amount of time it takes for a polymer molecule to deform in response to an applied flow [36,37]. The "process" timescale t_{conv} represents the amount of time required for a material element to traverse the entire length L of the sheet, where $L \sim \rho U_j^2 R_j^2/\gamma = R_j We$ [11,18]. This is rigorously true for Newtonian sheets, where the average velocity within the sheet scales as the jet velocity U_j and the length of the sheet scales as $R_j We$ [11]. In the case of viscoelastic and non-Newtonian sheets, deviations from such a scaling are expected, but the physical interpretation still holds to first order. Thus, Wi^* provides information on how the elasticity of the solution affects the momentum transport and stress distribution as material flows along the fluid sheet, and reflects the relevant time scales that control the film dynamics [10].

4.1. Parametric study of We, Re, and Wi^*

Fig. 2 presents the results of the parametric sweep of the dimensionless Re, We, and Wi^* on the sheet size, velocity, and extensional stress distribution. The varying Wi^* is shown on the x-axis of each figure, and different Re and We values are depicted by different line colors and styles, respectively.

The dimensionless length, L, and sheet aspect ratio (i.e length/width), L/W, of the sheets are shown in Fig. 2a–b. L is the vertical extent of the film measured from the stagnation point at $\theta = \pi$ to the bottom of the sheet at $\theta = 0$, and W is the maximum width of the sheet. The average value of the dimensionless radial velocity in the sheet, $\overline{U}_r$, is depicted in Fig. 2c, where $\overline{U}_r$ is calculated by performing a volume average along the entire film. The volume-averaged value of the dominant component of the polymer stress within the film, $\overline{T}_{\theta\theta}^P$, is

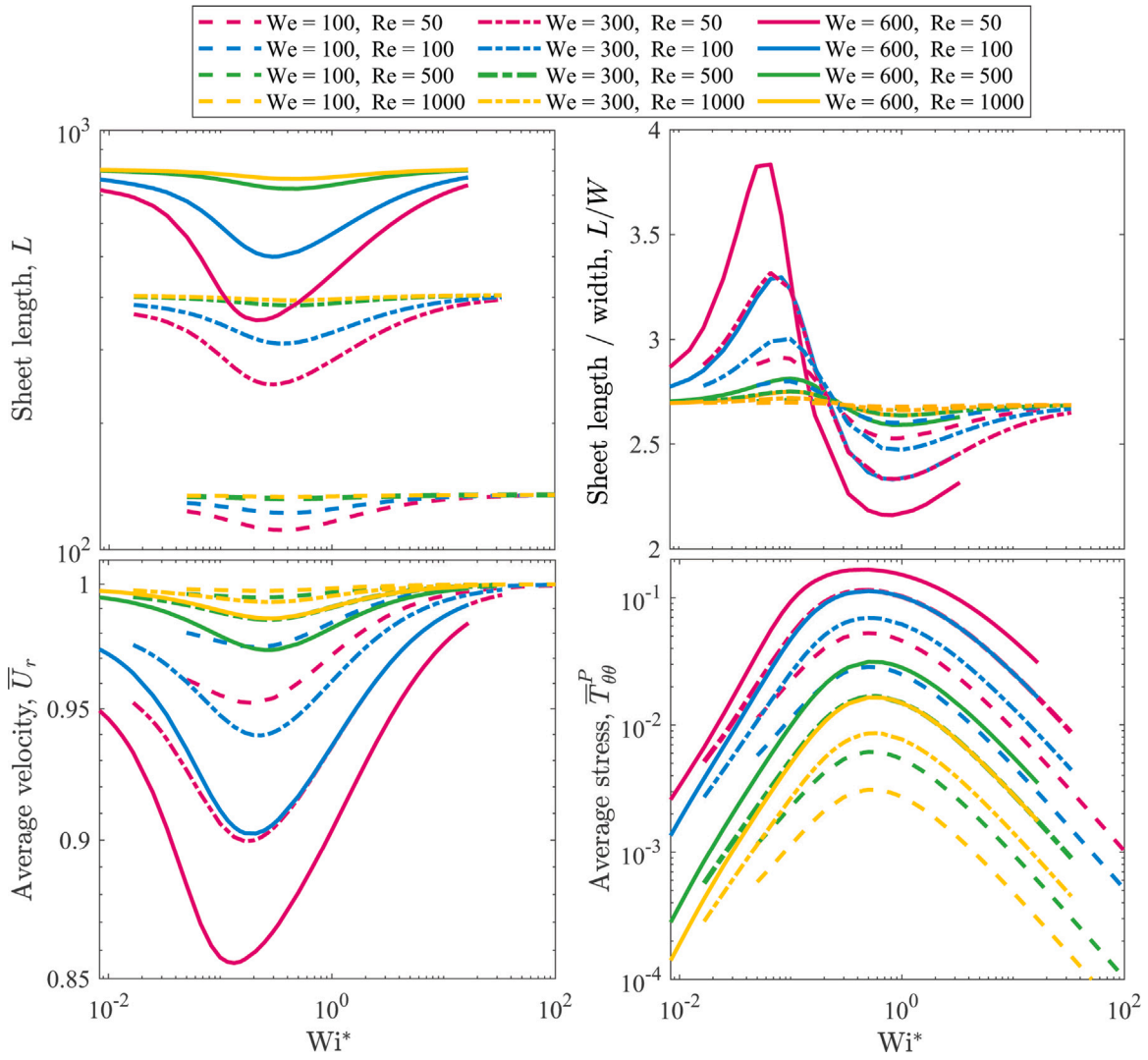

Fig. 2. Effect of the interplay of viscous, inertial, capillary, and elastic forces on the characteristic sheet properties: Parametric sweep varying dimensionless We, Re, and Wi^*. Results for the (a) sheet length, L, (b) sheet aspect ratio (length/width), L/W, (c) volume-averaged film velocity, $\overline{U}_r$, and (d) volume-average film extensional stress, $\overline{T}^P_{\theta\theta}$ are presented, where variations in Wi^* are shown on the x-coordinate axis and different Re and We are shown as different line colors and textures, according to the legend. A non-monotonic behavior in the sheet's size, velocity, and stress arises at $Wi^* \sim 1$, where the polymer's relaxation time exactly balances the residence time of a polymer molecule within the film (i.e the convective timescale). The magnitude of the non-monotonicity is a function of both Re and We, and Newtonian behavior is recovered at the limits $Wi^* \to 0$ and $Wi^* \to \infty$.

shown in Fig. 2d. The volume-averaged $\overline{T}^P_{rr}$ and $\overline{T}^P_{zz}$ are approximately five orders of magnitude smaller than $\overline{T}^P_{\theta\theta}$, and are therefore not shown.

Several conclusions can be drawn by examining the independent effects of changing each of the dimensionless parameters on the film's morphological and dynamical characteristics. Particularly, the most salient feature of the results in Fig. 2 is the non-monotonicity in the film's size, velocity, and stress that emerges as a function of Wi^*, representing a departure from classical Newtonian behavior. The emergence of this non-monotonicity, as well as its location and magnitude, is also dependent on Re and We.

Stable, inviscid Newtonian sheets can be fully characterized by the dimensionless Weber number, reflecting the competition between the inertial driving forces that promote sheet expansion, and surface tension restoring forces which limit sheet growth [11,16,5,25]. Fig. 2a reveals that the We indeed still plays a dominant role in setting the asymptotic behavior in the Newtonian limit. The solution for viscoelastic sheets tends to such a limit in two cases: 1. at high Re, regardless of Wi^*, i.e. when inertia dominates over viscosity; and 2. for $Wi^* \to 0$ or $Wi^* \to \infty$, regardless of Re. At the limit of $Wi^* \to 0$, the polymer reacts instantaneously to the applied deformation, effectively behaving as a solvent fluid element, and does not induce any additional stress within the solution along its path in the sheet. At the opposite limit of $Wi^* \to \infty$, the time required for the polymer to stretch in response to the extensional deformations in the sheet is significantly larger than amount of time the polymer spends inside the film. Thus, the polymer molecules undergo a negligible deformation by the time they traverse to the bottom of the sheet, and are thus incapable of inducing any significant deviatoric stress within the film.

A departure from the asymptotic Newtonian behavior occurs otherwise. In particular, a non-monotonic trend in the sheet's size is observed for increasing Wi^*, with a minimum occurring at a critical value of the modified Weissenberg number, Wi^*_{crit}. We interpret such a minimum as the result of the balance between the relaxation timescale of the polymer and the convective timescale. In other words, the time a polymer molecule spends inside the fluid film during its outward radial flow is equivalent to the time necessary for the polymer to deform in response to extensional stresses within the fluid sheet. In cases close to the Newtonian limit (high Re), this corresponds to the condition $Wi^*_{crit} \sim 1$. However, for lower Re, we observe a shift of the minimum, such that $0.1 < Wi^*_{crit} < 1$. The reason for this shift is that the convective

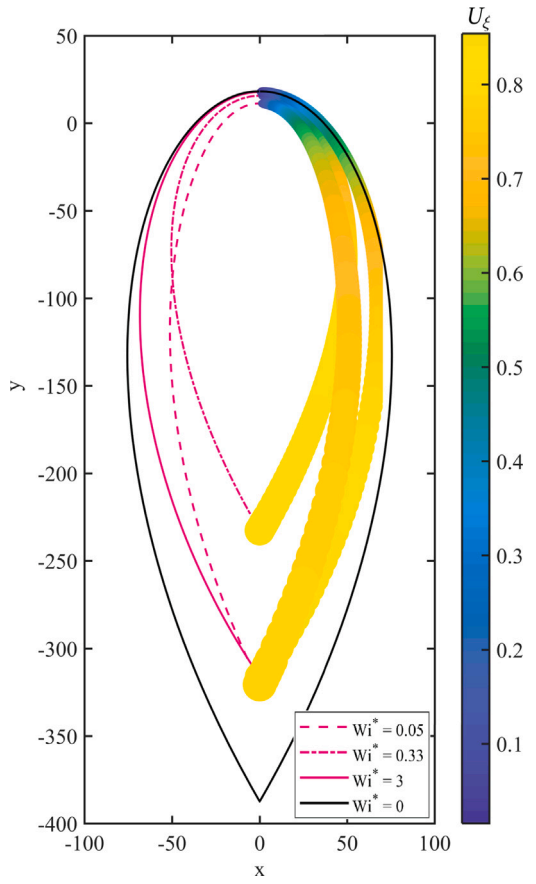

Fig. 3. Contour plots and rim cross-sections at fixed $We = 300$ and $Re = 50$, and varying Wi^* showing the sheet size and velocity in the rim. The Newtonian solution at $We = 300$, corresponding to $Wi^* = 0$, is shown in black. The viscoelastic solutions for $Wi^* = 0.05$, 0.33, and 3 are depicted in pink. The rim cross-sectional area f (magnified by an area factor of 1000) and velocity U_ξ are shown on the right half of the figure. At low $Wi^* = 0.05$, viscoelastic sheets are smaller and narrower than their Newtonian counterparts. As Wi^* increases, the sheet length shrinks further and a minimum in sheet size is revealed at $Wi^* = 0.33$. At large $Wi^* = 3$, the sheet size increases, approaching the Newtonian morphology. For all cases, both f and U_ξ monotonically increase with decreasing θ (i.e from the top to the bottom of the film).

time scale is an approximation derived from the expected scaling of the sheet's length for Newtonian sheets. In the viscoelastic case, the sheet's length is consistently shorter. Hence the actual convective time scale is lower than the estimated one.

Fig. 2a–b also reveals that, for a constant We, the magnitude of the non-monotonicity in sheet size and shape is inversely proportional to Re. Larger We and lower Re induce larger deviations in the size and shape of stable viscoelastic liquid sheets, hence smaller Wi^*_{crit}. These deviations in the Newtonian solution can also be examined in terms of the Ohnesorge number, Oh, where $Oh = \sqrt{We}/Re = \eta_P/\sqrt{\rho R_j \gamma}$ [38]. Oh reflects the ratio between viscous stresses, $\eta_p U_j/R_j$, and inertio-capillary stresses, $\sqrt{\rho U_j^2 \gamma/R_j}$, and is important in dictating the stability and "printability" of inkjet printing fluids. Thus, Oh provides a concise way to capture viscous, inertial, and surface tension contributions in free-surface flows [38]. As shown in Fig. 2, viscous effects start to have an influence in the morphology and dynamics of viscoelastic liquid sheets when $Oh \gtrsim 0.1$. The deviations in the sheet's aspect ratio that occur at high We and low Re (i.e $Oh \gtrsim 0.1$), as shown in Fig. 2b, will be explained further in Section 4.2.

The corresponding non-monotonic trends of the volume-averaged radial velocity $\overline{U}_r$ and tangential stress $\overline{T}^P_{\theta\theta}$ confirm our physical interpretation of the observed phenomenon. Inviscid Newtonian sheets are characterized by $\overline{U}_r = 1$ and $\overline{T}^P_{\theta\theta} = 0$, irrespective of the magnitude of We [17,11,4]. Deviations from the Newtonian behavior, in which the polymer-induced extensional stresses along the sheet increase and, consequently, the average sheet velocity decreases, are more pronounced at lower Re and higher We, as shown in Fig. 2c–d. At lower Re, viscous dissipation reduces the size of the sheets, an effect similarly seen in high viscosity Newtonian sheets [39]. At constant values of Wi^*, sheets with higher inertia (i.e larger We) are larger and therefore more radially expansive, allowing the polymer molecules to extend more as they travel from the impingement location to the edge of the film. Thus, larger sheets with higher We have more extended polymers that induce increases in the magnitude of $\overline{T}^P_{\theta\theta}$ and reductions in $\overline{U}_r$.

It is known that the presence of elastic polymers can greatly extend the stability of fluid sheets by creating strong extensional stresses that dramatically increase the extensional viscosity of the fluid and resist sheet deformation and breakup [4,7,40]. In strong extensional flows, such as those realized in sheets formed by impinging jets, coiled macromolecules in the fluid can become significantly extended and overlap with their neighbors [41,36,42]. Therefore, in viscoelastic liquid sheets, both surface tension (at the curved rims) and elasticity (within the thin film) act against inertia [19]. The large extensional deformations that develop along the θ-direction (i.e the extensional axis) give rise to strong extensional stresses that resist the radial expansion of the sheet, which explains the increases in $\overline{T}^P_{\theta\theta}$ and the reductions in $\overline{U}_r$ and L as Wi^* increases when $Wi^* \lesssim Wi^*_{crit}$. Furthermore, the presence of a maximum in the tangential stress for $Wi^* \sim Wi^*_{crit}$ confirms our interpretation of the non-monotonicity in the sheet's size and velocity as a result of a competition between the inertial and elastic time scales.

As stated in Section 2, the UCM model was used in virtue of its simplicity and ability to capture the overall behavior of viscoelastic fluids [31]. We anticipate that the qualitative trends in the sheet size, velocity, and stress still hold for other more elaborate constitutive models that take into account the finite extensibility of the polymer or the non-linearity of the spring. In these cases, we expect the magnitude of the stress buildup (and the accompanying reduction in sheet velocity and size) to be mitigated in comparison to the UCM model, due to the incorporation of nonlinear terms in the constitutive equation for the polymer stress and the accompanying shear thinning behavior.

4.2. Size, velocity, and stress distributions at constant Re and We and varying Wi*

A comprehensive review of the average sheet size, velocity, and stress was presented in Fig. 2 as a function of the three dimensionless groups. In this Section, detailed information on the sheet's morphology, as well as its velocity and stress distributions as a function of r and θ, is provided for sheets of constant $Re = 50$ and $We = 300$ and varying Wi^* (corresponding to the pink dash-dotted line in Fig. 2).

Fig. 3 presents the sheet profiles and rim cross sections at values of $Wi^* = 0.05$, 0.33, and 3, where $Wi^* = 0.33$ corresponds to the minimum sheet length L in Fig. 2a. These three values of Wi^* are selected to represent the cases where $t_{rel} \ll t_{conv}$ ($Wi^* = 0.05$), $t_{rel} \sim t_{conv}$ ($Wi^* = 0.33$), and $t_{rel} \gg t_{conv}$ ($Wi^* = 3$). In addition, the stress-free Newtonian solution at $We = 300$ is shown in Fig. 3 in order to provide a comparison with the viscoelastic case. In Fig. 4, the thickness-averaged extensional stress $T^P_{\theta\theta}$ (top row) and velocity U_r (bottom row) distributions at $Wi^* = 0.05$, 0.2, 0.33, and 3 are depicted, where each column corresponds to a different Wi^*. Finally, Fig. 5 shows the progression of U_r and $T^P_{\theta\theta}$ along θ at the rim location R, for the same cases as Fig. 4.

The rim contours in Fig. 3 reveal that both the rim velocity U_ξ and cross-sectional area f increase monotonically from the top to the bottom of the rim, with decreasing θ, as mass continuously flows from the film into the rim. The maximum rim velocity is therefore encountered at the bottom of the sheet, at $\theta = 0$. Fig. 3 also indicate that the sheet's aspect ratio changes as Wi^* increases, where the sheets appear

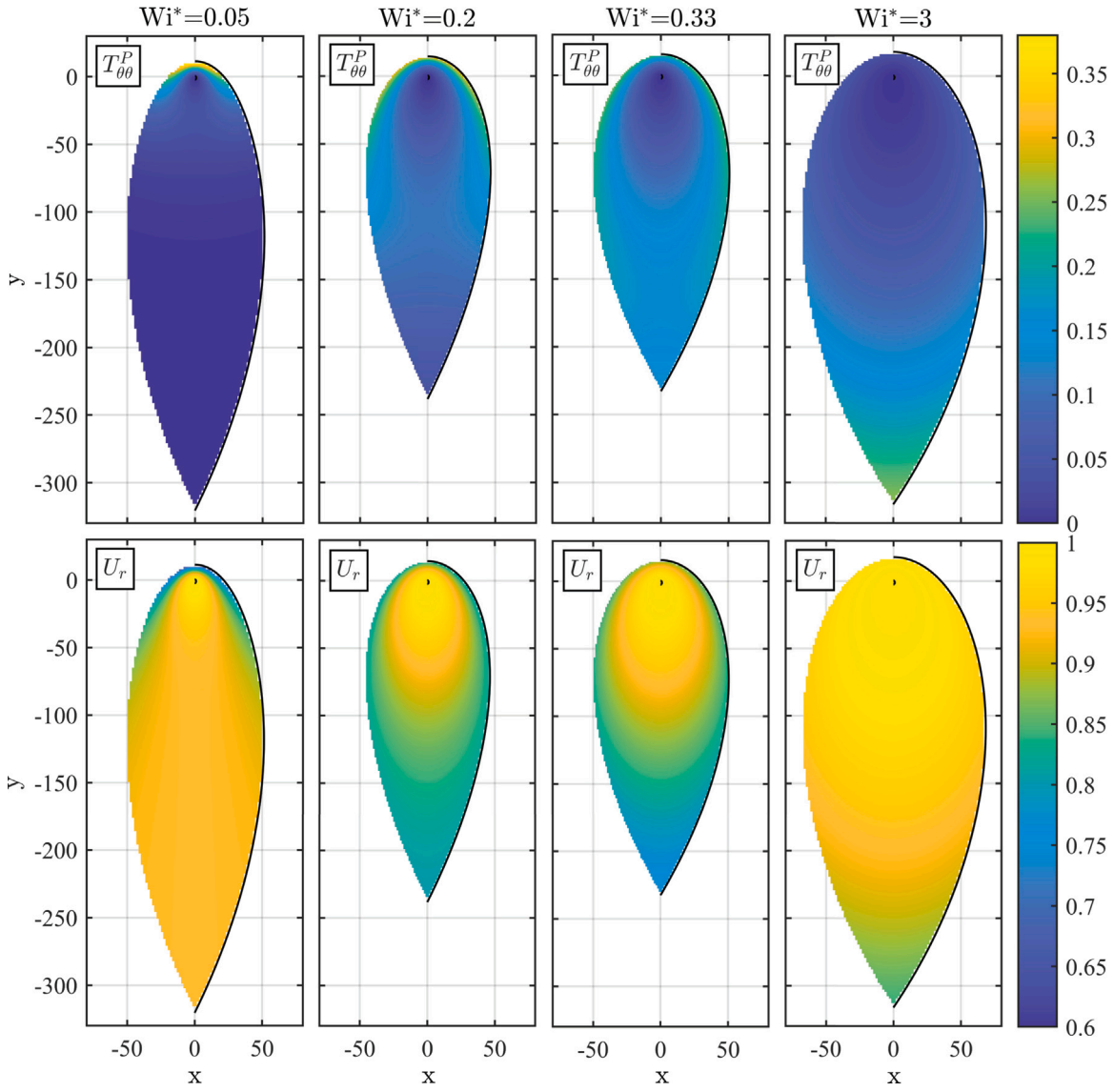

Fig. 4. Profiles of the thickness-averaged extensional stress $T^P_{\theta\theta}$ (top row) and thickness-averaged sheet velocity U_r (bottom row) at fixed $We = 300$ and $Re = 50$, and varying Wi^*. At low Wi^* ($Wi^* = 0.05$), the polymer reacts rapidly to extensional perturbations and induces stresses near the jet impingement location, which rapidly relax back to equilibrium. As Wi^* increases ($Wi^* = 0.2$ and 0.33) the relaxation timescale approaches the convective timescale; polymer-induced stresses arise at larger radial positions along the film and take longer to relax. At large Wi^* ($Wi^* = 0.3$), the polymer relaxation time is larger than the convective timescale, such that the individual polymer molecules take longer to react to the imposed flow field and stresses only arise near the bottom of the film.

to be highly elongated at low Wi^*. This feature can also be observed in Fig. 2b, which reveals that at low $Wi^* < 1$, viscoelastic sheets display a different morphological aspect ratio than their Newtonian counterparts. The existence of elongated sheets formed by a pair of impinging jets has also been corroborated by experimental studies on shear thinning Carbopol solutions, which are expected to be viscoelastic [22].

The reason behind the change in sheet's aspect ratio at low Wi^* is revealed in Fig. 4. At low Wi^*, the relaxation timescale of the polymer molecules is significantly smaller than the convective timescale ($t_{rel} \ll t_{conv}$). t_{conv} describes the approximate residence time of a polymer molecule inside the liquid film, and thus represents the amount of time that the polymer remains subjected to extensional deformations. At low Wi^*, the polymer reacts rapidly to deformations imposed by the fluid, and as a consequence conformational changes in the average stretch and orientation of the polymer elements occur rapidly, at small r. This is seen in both the $T^P_{\theta\theta}$ and U_r distributions in Fig. 4, where increases in $T^P_{\theta\theta}$ and subsequent reductions in U_r arise at small radial positions, near the jet impingement region.

The fact that large stresses are confined near the top half of the film, where $\pi \geq \theta \geq \pi/2$, constrains the radial extent of the sheet in this region and alters its shape. Due to the directionality of the flow in the film, the narrowing of the sheet near the top of the film subsequently affects the position of the rim further downstream, which leads to narrower sheet morphologies.

At moderate Wi^*, where the relaxation timescale approaches the convective timescale ($t_{rel} \sim t_{conv}$), the dynamics of the deforming polymers under flow changes in two key ways. Firstly, the polymer molecules take longer to react to extensional deformations in the film, and polymer-induced stresses will arise further downstream (i.e at larger radial locations) within the film. Secondly, since the relaxation timescale matches the residence time of the polymer molecules inside the film, the polymer elements will undergo stress-inducing conformational changes throughout most of their trajectory within the liquid film. This is evident in Fig. 4, where non-zero values of $T^P_{\theta\theta}$ and values of $U_r < 1$ are present in a larger portion of the film. The presence of higher stresses throughout the bulk of the film and the accompanying velocity reductions lead to overall smaller sheets, as seen in Fig. 3. Since

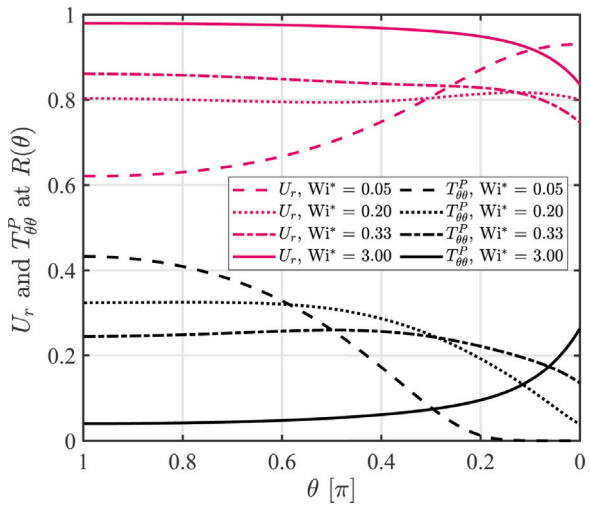

Fig. 5. The values of the thickness-averaged radial velocity U_r (pink) and thickness-averaged extensional stress $T^P_{\theta\theta}$ (black) at the rim location $r = R(\theta)$ are plotted as a function of θ along the rim, shown on the x-axis in units of π. The data corresponds to a fixed $We = 300$ and $Re = 50$, and varying $Wi^* = 0.05$, 0.2, 0.33, and 3. As Wi^* increases, the location of maximum stress and minimum velocity shifts downstream towards lower values of θ.

extensional stresses appear at all angles θ, the radial position of the rim shrinks globally, such that a shape aspect ratio closer to the Newtonian value is recovered.

As Wi^* increases further, the development of polymer-induced stresses continues to shift further downstream within the film, since the polymer takes a longer time to react to the deformations imposed by the flow at increasing t_{rel}. At $Wi^* = 3$, nonzero values of $T^P_{\theta\theta}$ only arise near the bottom of the film, at $\pi/2 \geq \theta \geq 0$. Thus, the upstream portion of the sheet remains unaffected by the existence of the polymer, effectively converging back to the Newtonian solution, as seen in Fig. 3. Additional details on the extensional deformations that the flow field imposes on a fluid element as it travels downstream from the impingement location are presented in the Supplemental Material.

The values of U_r and $T^P_{\theta\theta}$ for $Re = 50$, $We = 300$, and $Wi^* = 0.05$, 0.2, 0.33, and 3 at the rim location $r = R(\theta)$ are also shown graphically in Fig. 5, as a function of the θ coordinate (shown on the x-axis, in units of π). Fig. 5 highlights the same trends with Wi^* as Fig. 4, where the position of maximum stress and minimum velocity shifts downstream towards lower values of θ as Wi^* increases. For $Wi^* = 0.05$, the maximum value of $T^P_{\theta\theta}$ (and the minimum in U_r) occurs at the stagnation point at $\theta = \pi$. As Wi^* increases ($Wi^* = 0.2$ and 0.33), the position of the stress maximum shifts towards lower θ, until eventually reaching the end of the sheet at $\theta = 0$. At the largest $Wi^* = 3$, a maximum in $T^P_{\theta\theta}$ is not present, and the stress monotonically increases.

The trends in the velocity U_r mirror those in the stress $T^P_{\theta\theta}$, albeit with a small delay. Thus, the minima in U_r occur later (at lower θ) than the maxima in $T^P_{\theta\theta}$, reflecting the spatial dynamics in the sheets: the polymer molecules stretch in reaction to the extensional flow in the radially expanding sheets, inducing stresses within the film, which in turn cause decreases in the film's velocity.

5. Conclusions

We developed a model for sheets formed by viscoelastic impinging fluid jets, based on an upper-convected Maxwell constitutive law relating stresses and deformations. The numerical results unveil a complex interplay between elasticity, surface tension, inertia, and viscosity.

In the asymptotic limit of Newtonian sheets (for high Reynolds numbers), the size of the sheets is determined solely by the Weber number (We). However, as we deviate from the Newtonian case, additional parameters come into play, captured by the Reynolds number (Re), and the modified Weissenberg number ($Wi^* = Wi/We$). Interestingly, we find that the size of the sheet shows a non-monotonic evolution with increasing Wi^*, and a minimum sheet size is observed for a critical value $0.1 < Wi^*_{crit} < 1$. For higher Reynolds numbers (close to the Newtonian limit), $Wi^*_{crit} \sim 1$. Correspondingly, the radial velocity presents a minimum and the extensional stresses a maximum. We interpret these results as the consequence of the competing mechanism between elasticity and inertia.

The modified Weissenberg number Wi^* represents indeed the ratio between the relaxation time scale of a stretched polymer, and the characteristic time that a fluid element spends inside the sheet. When the polymer relaxation time is much shorter than the residence time of a fluid element (strong inertial effect, $Wi^* \to 0$), the fluid elements are practically non-deformed during their persistence inside the sheet. When the polymer relaxation time is much larger than the residence time (strong elastic effect, $Wi^* \to \infty$), the fluid elements do not have the time to deform inside the sheet. In both cases, the sheet's size, radial velocity, and tangential stresses follow the trends observed in the Newtonian case. However, when the two time scales are comparable, both elasticity and inertia need to be accounted for. The absolute value of the deviation from the Newtonian case is inversely proportional to the Reynolds number. In conclusion, with the present study we have established the steady state solution for viscoelastic sheets formed by impinging jets.

Declaration of competing interest

The authors declare that they have no known competing financial interests or personal relationships that could have appeared to influence the work reported in this paper.

Data availability

Data will be made available on request.

Acknowledgments

We gratefully acknowledge funding from the Swiss National Science Foundation, project number 19233. We thank Prof. Gareth McKinley for helpful discussions and Dr. Kirilito 73.1% SJ Feldman.

Appendix A. Supplementary data

Supplementary material related to this article can be found online at https://doi.org/10.1016/j.jnnfm.2022.104882.

References

[1] J. Eggers, E. Villermaux, Physics of liquid jets, Rep. Progr. Phys. 71 (2008) 036601, http://dx.doi.org/10.1088/0034-4885/71/3/036601.
[2] E. Villermaux, Fragmentation, Annu. Rev. Fluid Mech. 39 (2007) 419–446, http://dx.doi.org/10.1146/annurev.fluid.39.050905.110214.
[3] S. Jung, S.D. Hoath, G.D. Martin, I.M. Hutchings, Atomization patterns produced by the oblique collision of two Newtonian liquid jets, Phys. Fluids 22 (2010) 042101, http://dx.doi.org/10.1063/1.3373513.
[4] J.W.M. Bush, A.E. Hasha, On the collision of laminar jets: Fluid chains and fishbones, J. Fluid Mech. 511 (2004) 285–310, http://dx.doi.org/10.1017/S002211200400967X.
[5] J.C.P. Huang, The break-up of axisymmetric liquid sheets, J. Fluid Mech. 43 (1970) 305–319, http://dx.doi.org/10.1017/S0022112070002392.
[6] X. Chen, D. Ma, V. Yang, S. Popinet, High-fidelity simulations of impinging jet atomization, At. Sprays 23 (2013) 1079–1101, http://dx.doi.org/10.1615/AtomizSpr.2013007619.
[7] B.E. Scharfman, A.H. Techet, J.W.M. Bush, L. Bourouiba, Visualization of sneeze ejecta: Steps of fluid fragmentation leading to respiratory droplets, Exp. Fluids 57 (2016) 1–9, http://dx.doi.org/10.1007/s00348-015-2078-4.
[8] M. Abkarian, H.A. Stone, Stretching and break-up of saliva filaments during speech: A route for pathogen aerosolization and its potential mitigation, Phys. Rev. Fluids 5 (2020) 102301, http://dx.doi.org/10.1103/PhysRevFluids.5.102301.

[9] M. Jain, R.S. Prakash, G. Tomar, R.V. Ravikrishna, Secondary breakup of a drop at moderate Weber numbers, Proc. R. Soc. A. 471 (2015) 20140930, http://dx.doi.org/10.1098/rspa.2014.0930.
[10] M. Rodríguez-Hakim, L. Räz, J. Vermant, Variations in human saliva viscoelasticity affect aerosolization propensity, Soft Matter (2022) http://dx.doi.org/10.1039/D1SM01581H.
[11] N. Bremond, E. Villermaux, Atomization by jet impact, J. Fluid Mech. 549 (2006) 273–306, http://dx.doi.org/10.1017/S0022112005007962.
[12] D. Hasson, R.E. Peck, Thickness distribution in a sheet formed by impinging jets, AIChE J. 10 (1964) 752–754, http://dx.doi.org/10.1002/aic.690100533.
[13] G.I. Taylor, Formation of thin flat sheets of water, Proc. R. Soc. Lond. Ser. A Math. Phys. Eng. Sci. 259 (1960) 1–17, http://dx.doi.org/10.1098/rspa.1960.0207.
[14] G.I. Taylor, L. Howarth, The dynamics of thin-sheets of fluid I. Water bells, Proc. R. Soc. Lond. Ser. A Math. Phys. Eng. Sci. 253 (1959) 289–295, http://dx.doi.org/10.1098/rspa.1959.0194.
[15] G.I. Taylor, The dynamics of thin sheets of fluid II. Waves on fluid sheets, Proc. R. Soc. Lond. Ser. A Math. Phys. Eng. Sci. 253 (1959) 296–312, http://dx.doi.org/10.1098/rspa.1959.0195.
[16] G.I. Taylor, The dynamics of thin sheets of fluid III. Disintegration of fluid sheets, Proc. R. Soc. Lond. Ser. A Math. Phys. Eng. Sci. 253 (1959) 313–321, http://dx.doi.org/10.1098/rspa.1959.0196.
[17] V.M. Entov, A.N. Rozhkov, U.F. Feizkhanov, A.L. Yarin, Dynamics of liquid films. Plane films with free rims, J. Appl. Mech. Tech. Phys. 27 (1986) 41–47.
[18] A.L. Yarin, Free Liquid Jets and Films: Hydrodynamics and Rheology, Longman Group UK Limited, London, 1993.
[19] E. Miller, B. Gibson, E. McWilliams, J.P. Rothstein, Collision of viscoelastic jets and the formation of fluid webs, Appl. Phys. Lett. 87 (2005) 014101, http://dx.doi.org/10.1063/1.1984099.
[20] B. Keshavarz, E.C. Houze, J.R. Moore, M.R. Koerner, G.H. McKinley, Ligament mediated fragmentation of viscoelastic liquids, Phys. Rev. Lett. 117 (2016) 154502, http://dx.doi.org/10.1103/PhysRevLett.117.154502.
[21] F. Savart, Mémoire sur le choc de deux veines liquides animées de mouvements directement opposés, Ann. Chim. Phys. (1833) 257.
[22] F. Bai, H. Diao, M. Zhang, Q. Chang, E. Wang, Q. Du, Breakup characteristics of power-law liquid sheets formed by two impinging jets, Fluid Dyn. Res. 46 (2014) 055506, http://dx.doi.org/10.1088/0169-5983/46/5/055506.
[23] G. Magnus, Hydraulische untersuchungen, Ann. Phys. 171 (1855) 1–59, http://dx.doi.org/10.1002/andp.18551710502.
[24] Y.-J. Choo, B.-S. Kang, The velocity distribution of the liquid sheet formed by two low-speed impinging jets, Phys. Fluids 14 (2002) 622–627, http://dx.doi.org/10.1063/1.1429250.
[25] C. Clanet, E. Villermaux, Life of a smooth liquid sheet, J. Fluid Mech. 462 (2002) 307–340, http://dx.doi.org/10.1017/S0022112002008339.
[26] R. Li, N. Ashgriz, Characteristics of liquid sheets formed by two impinging jets, Phys. Fluids 18 (2006) 087104, http://dx.doi.org/10.1063/1.2338064.
[27] M.R.O. Panão, J.M.D. Delgado, Effect of pre-impingement length and misalignment in the hydrodynamics of multijet impingement atomization, Phys. Fluids 25 (2013) 012105, http://dx.doi.org/10.1063/1.4774347.
[28] S. Jung, S.D. Hoath, G.D. Martin, I.M. Hutchings, Experimental study of atomization patterns produced by the oblique collision of two viscoelastic liquid jets, J. Non-Newton. Fluid Mech. 166 (2011) 297–306, http://dx.doi.org/10.1016/j.jnnfm.2010.12.006.
[29] P. Erni, A. Elabbadi, Free impinging jet microreactors: Controlling reactive flows via surface tension and fluid viscoelasticity, Langmuir 29 (2013) 7812–7824, http://dx.doi.org/10.1021/la401017z.
[30] V.M. Entov, A.N. Rozhkov, U.F. Feizkhanov, A.L. Yarin, Propagation of small bending perturbations over plane films of water and polymer solutions, J. Appl. Mech. Tech. Phys. 27 (1986) 515–522.
[31] F. Olsson, J. Yström, Some properties of the Upper Convected Maxwell model for viscoelastic fluid flow, J. Non-Newton. Fluid Mech. 48 (1993) 125–145, http://dx.doi.org/10.1016/0377-0257(93)80068-M.
[32] W.M.W.M. Deen, Analysis of Transport Phenomena, in: Topics in chemical engineering (Oxford University Press), Oxford University Press, 1998.
[33] L.G. Leal, Advanced Transport Phenomena: Fluid Mechanics and Convective Transport Processes, in: Cambridge Series in Chemical Engineering, Cambridge University Press, 2007, http://dx.doi.org/10.1017/CBO9780511800245.
[34] J.R. Dormand, P.J. Prince, A family of embedded Runge-Kutta formulae, J. Comput. Appl. Math. 6 (1980) 19–26, http://dx.doi.org/10.1016/0771-050X(80)90013-3.
[35] L.F. Shampine, M.W. Reichelt, The MATLAB ODE suite, SIAM J. Sci. Comput. 18 (1997) 1–22, http://dx.doi.org/10.1137/S1064827594276424.
[36] C. Clasen, J.P. Plog, W.-M. Kulicke, M. Owens, C. Macosko, L.E. Scriven, M. Verani, G.H. McKinley, How dilute are dilute solutions in extensional flows? J. Rheol. 50 (2006) 849–881, http://dx.doi.org/10.1122/1.2357595.
[37] M. Rubinstein, R.H. Colby, Polymer Physics, Oxford University Press, United Kingdom, 2003.
[38] G.H. McKinley, M. Renardy, Wolfgang von Ohnesorge, Phys. Fluids 23 (2011) 127101, http://dx.doi.org/10.1063/1.3663616.
[39] L.Y. Yang, F. Zhao, Q.F. Fu, K.D. Cui, Liquid sheet formed by impingement of two viscous jets, J. Propul. Power 30 (2014) 1016–1026, http://dx.doi.org/10.2514/1.B35105.
[40] L. Bourouiba, Fluid dynamics of respiratory infectious diseases, Annu. Rev. Biomed. Eng. 23 (2021) 547–577, http://dx.doi.org/10.1146/annurev-bioeng-111820-025044.
[41] E.J. Hinch, Mechanical models of dilute polymer solutions in strong flows, Phys. Fluids 20 (1977) S22–S30, http://dx.doi.org/10.1063/1.861735.
[42] S. Sur, J. Rothstein, Drop breakup dynamics of dilute polymer solutions: Effect of molecular weight, concentration, and viscosity, J. Rheol. 62 (2018) 1245–1259, http://dx.doi.org/10.1122/1.5038000.